PCCP

PAPER

# Remarkable hydrogen storage properties of $MgH_2$ doped with $VNbO_5$

Cite this: DOI: 10.1039/c7cp07157d

Antonio Valentoni, *[a] Gabriele Mulas,[a] Stefano Enzo[a] and Sebastiano Garroni[bc]

The present work concerns the catalytic effect of $VNbO_5$, a ternary oxide prepared *via* a solid-state route, on the sorption performance of $MgH_2$. Three doped systems, namely 5, 10 and 15 wt% $VNbO_5$–$MgH_2$ have been prepared by ball milling and thoroughly characterized. Hydrogen sorption, evaluated by temperature programmed desorption experiments, revealed a significant reduction of the desorption temperature from 330 °C for the un-doped sample (prepared and tested for comparison) to 235 °C for the $VNbO_5$-doped sample. Furthermore, more than 5 wt% of hydrogen can be absorbed in 5 minutes at 160 °C under 20 bar of hydrogen, which is remarkable compared to the 0.7 wt% achieved for the un-doped system. The sample doped with 15 wt% of additive, showed good reversibility: over 5 wt% of hydrogen with negligible degradation even after 70 consecutive cycles at 275 °C and 50 cycles at 300 °C. The kinetics analysis carried out by Kissinger's method exhibited a considerable reduction of the activation energy for the desorption process. Finally, pressure-composition-isotherm experiments conducted at three different temperatures allowed estimating the thermodynamic stability of the system and shed light on the additive role of $VNbO_5$.

Received 21st October 2017,
Accepted 4th January 2018

DOI: 10.1039/c7cp07157d

rsc.li/pccp

## Introduction

The use of hydrogen as a carbon-free energy vector is one of the most suitable technological challenges for mitigating the carbon dioxide emissions caused by the extensive exploitation of carbon fossil fuels.[1] Commercialization of hydrogen fuel cell vehicles (FCVs) represents, for example, a "greener" and efficient alternative to the gasoline internal combustion engine (ICE) responsible for 17% of the total $CO_2$ emission in the EU (2008). However, in order to promote a rapid diffusion of this technology into the global market, obstacles related to the storage and the transport of hydrogen have to be overcome. The most exploited solutions such as hydrogen liquid and a high-pressure tank, suffer from high costs and safety constraints which limit their utilization in several countries.[2]

Based on these considerations the search for an efficient, safe and less expensive hydrogen storage approach is becoming of primary importance. Solid-state hydrogen storage has potential advantages in terms of volumetric density and safety compared to the pressurized gas technology.[3] In this framework, vast numbers of materials have been investigated in order to find a valid candidate able to ab/de-sorb reversibly hydrogen at moderate temperatures, satisfying the DOE requirements.[4–6] Among them, the $MgH_2$ system remains one of the most studied and interesting compounds for solid-state hydrogen storage, due to its high gravimetric capacity of 7.6 wt% combined with a relatively cheap cost (<3 € per kg) and abundance (7th element on Earth).[7] However, it has several limitations for practical application, for example a very high desorption temperature of 400–450 °C and slow kinetics at temperatures below 400 °C.[8,9] Various strategies have been proposed in order to improve the hydrogen sorption properties of $MgH_2$, and, among them, the combination with other complex hydrides[10–14] and the doping with metals,[15–18] metal halides[19–21] and metal oxides,[22–26] probably represent the most successful approaches reported in the current literature.

The addition of metal oxides, in particular, produced a clear benefit in terms of hydrogen sorption kinetics and desorption temperature. Since the pioneering work of Barkhordarian *et al.*[22] which demonstrated the extraordinary catalytic effect of $Nb_2O_5$ on the $MgH_2$ sorption performance, much attention has been addressed to this additive.[22–26] To get an insight into the catalytic mechanism, *in situ* experiments have evidenced the crucial role played by the Mg–Nb oxide phases formed during the sorption reaction of the $Nb_2O_5$-doped $MgH_2$ system.[27] This ternary oxide, conversely to MgO, facilitates the diffusion of hydrogen into the Mg bulk and assists the hydrogen splitting reaction, thus improving the sorption

[a] Department of Chemistry and Pharmacy, Università degli Studi di Sassari e INSTM, Via Vienna 2, I-07100 Sassari, Italy. E-mail: avalentoni@uniss.it, mulas@uniss.it, enzo@uniss.it
[b] International Research Centre in Critical Raw Materials-ICCRAM, University of Burgos, Plaza Misael Banuelos s/n, 09001 Burgos, Spain. E-mail: sgarroni@ubu.es
[c] Advanced Materials, Nuclear Technology and Applied Bio/Nanotechnology, Consolidated Research Unit UIC-154, Castilla y Leon. Spain. University of Burgos, Hospital del Rey s/n, 09001 Burgos, Spain

properties of the whole system.[28] Friedrichs *et al.* demonstrated that the Mg–Nb oxide limits the grain growth of Mg during desorption preserving the grain boundaries for hydrogen diffusion. Further studies conducted using TEM, XPS and EDX showed that during mechanical treatment, the nanosized Nb oxide diffuses into the $MgH_2$ matrix and starts a reducing process of the Nb oxide.[29,30] During the heating treatment, Nb in the high valence state (V) was further reduced by Mg, forming various mixed Mg–Nb oxide compounds. The ability to easily change the oxidation number during the de/hydrogenation cycles, and the highly accessible valence state, facilitate the hydrogen transport into the Mg matrix reducing the kinetics barriers.[29,30] Among the Mg–Nb oxide families, only $Mg_3Nb_6O_{11}$ presented a reversible interaction with $H_2$.[31] This was ascribable to the crystal structure of the compound, characterized by the presence of octahedral niobium clusters inside the oxide lattice, different from the other Mg–Nb oxides investigated.[31]

From this specific literature, it emerges that the Nb-octahedral coordination geometry could play a key role in improving the hydrogen sorption properties of Mg-based systems. Similar microstructure properties were also satisfied in vanadium-doped Mg compounds with enhanced hydrogen storage properties.[32–34] However, despite the several numbers of additives tested, no data are reported in the current literature, to our knowledge, concerning a synergic effect of the V–Nb oxide phase characterized by octahedral clusters. A restricted number of stoichiometric and non-stoichiometric V–Nb–O compounds with different compositions have been studied sporadically, and their crystal structures have not always been determined unquestionably. Among them, only the $VNbO_5$ compound meets the local octahedral coordination criterion.[35–38]

Based on these considerations, the present investigation provides, for the first time, a detailed study of the effect of $VNbO_5$ on the sorption properties of magnesium hydride. The additive, prepared *via* the conventional route, is able to improve significantly the sorption properties of the system decreasing the desorption temperature and enhancing the cyclability of the whole system. The experimental methods are described in the following.

# Experimental

Commercial powders of $MgH_2$ (hydrogen storage grade) were purchased from Sigma-Aldrich, while crystalline $VNbO_5$ was prepared by prolonged annealing at 500 °C (2 h) of the pre-milled powders (200 h) containing a mixture of $V_2O_5$ (99%) and $Nb_2O_5$ (99%) in a 1 : 1 molar ratio. The $MgH_2$–$x$ wt% $VNbO_5$ ($x$ = 0, 5, 10 and 15) samples were then prepared by ball milling. For each system, 8 grams of powders were ball milled for 10 hours in a stainless steel vial with 2 balls (8 grams of each one).

All the mechanical treatments were performed using a Spex/Mixer mill model 8000, working at 875 rpm and under an inert Ar atmosphere. Manipulation of the samples was performed inside an MBraun glove box with $O_2$ and $H_2O$ levels $<1$ ppm.

The sorption properties of the samples were investigated by the temperature programmed desorption experiment (TPD) using a Sievert-based instrument Setaram PCT-Pro 2000 (pressure accuracy 1%). The composite was heated from room temperature to 400 °C at 5 °C $min^{-1}$ followed by an isothermal treatment for 2 h. A second desorption *via* heating up to 300 °C was carried out with the same modalities. All the experiments were carried out under static vacuum. The absorption performance was evaluated at 160 °C after submitting the sample to 20 bar of pure hydrogen for 3 h. After that, the sample was cooled to room temperature while maintaining a back pressure of 20 bar to prevent any desorption process. The life cycle experiment was performed after two activation dis-charging cycles: the dehydrogenated sample was measured at 250 °C, 275 °C and 300 °C under static vacuum, while 20 bar of hydrogen was applied for the absorption step. The Pressure-Composition-Isotherm (PCI) experiments were conducted after the cycle life experiment previously described. The measurement was carried out at 3 different temperatures of 275 °C, 300 °C and 325 °C, with pressures of 0–15 bar for the absorption, and 15–0 bar for the desorption steps. All measurements were conducted in the $\Delta p$ mode, using an increasing pressure of 1.5 bar per step (dwell time 90 min).

Calorimetric measurements of the as-milled powders were performed by using a Sensys DSC Setaram. The sample holder was charged with $\sim$50 mg of powder under an Ar atmosphere (1 bar) and the experiment conducted from room temperature to 500 °C. Five increasing heating rates were selected for the experiments, namely: 2 °C $min^{-1}$; 5 °C $min^{-1}$; 10 °C $min^{-1}$; 15 °C $min^{-1}$ and 20 °C $min^{-1}$.

Structural and microstructural characterization were performed by the X-ray powder diffraction technique, using a Rigaku Smart Lab with Bragg–Brentano geometry using Cu K$\alpha$ radiation (1.54178 Å) and a monochromator in the diffracted beam. For each analysis 0.3 grams of powder, stored in the glove box, was placed in an air-sensitive sample holder covered by an airtight hood of Kapton foil to prevent contact with air moisture and oxygen during the analysis. The microstructural parameters were then evaluated by fitting the XRPD patterns using the MAUD, a Rietveld refinement software.[39]

# Results and discussion

### Sorption and structural properties

The synthesis of $VNbO_5$ was successfully demonstrated by *ex situ* X-ray diffraction and reported in Fig. 1 together with the patterns of the un-milled (0 h) and milled (200 h) systems. The starting reagents were represented by the monoclinic $Nb_2O_5$ (ICSD 01-071-0005), space group $P2/m$, and the orthorhombic $V_2O_5$ (ICSD 01-072-0433) space group $Pmnm$. The XRD pattern of the composite after long milling treatment (200 h) was totally different, with the disappearance of the initial oxides and the presence of an amorphous phase together with the orthorhombic $Nb_{16.8}O_{42}$ (ICSD 01-071-0336) phase. After the thermal treatment at 500 °C, peaks ascribable to the crystalline

 

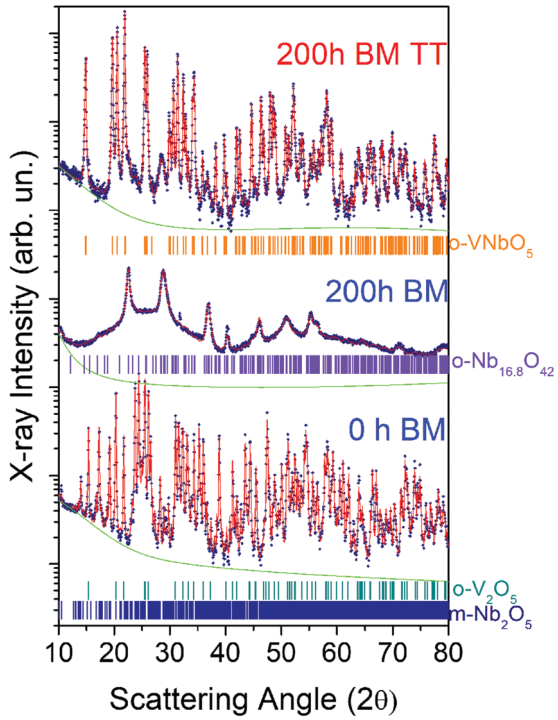


Fig. 1 XRD patterns and the corresponding interpolations of the equimolar mixture $V_2O_5$ and $Nb_2O_5$ un-milled (0 h BM, $R_{wp}$% 7.4), 200 h ball milled (200 h BM, $R_{wp}$% 4.2) and of the as-milled sample after the thermal treatment at 500 °C (200 h BM TT, $R_{wp}$% 5.6). In the bottom are reported the ticks of the crystalline phases present in the patterns. The experimental patterns, best fit profiles and backgrounds are represented by blue squares, red and green lines, respectively.

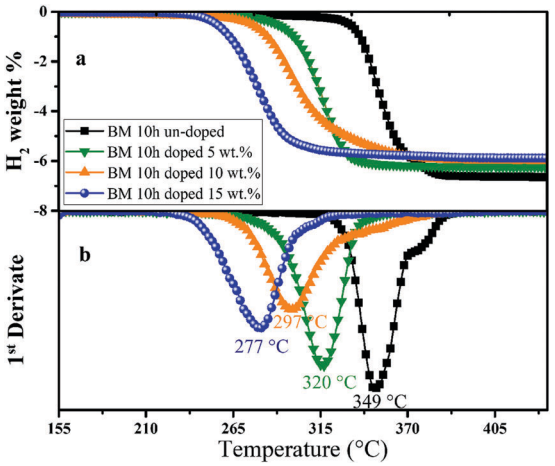


Fig. 2 (a) Temperature programmed desorption (TPD) profiles of the un-doped $MgH_2$ milled 10 h (dark squares) and of the $MgH_2$ systems milled (10 h) with 5 wt% (olive triangles), 10 wt% (orange triangles) and 15 wt% (blue circles) $VNbO_5$. (b) 1st derivate of the TPD measurements reported in panel (a).

VNbO5 (ICSD 00-046-0046) were observed together with $Nb_{16.8}O_{42}$ in trace (<5 wt%). The XRD pattern of $VNbO_5$ obtained by the solid-state route can be unambiguously identified and compared with previous data reported in the literature.[38]

Three different batches of pristine $MgH_2$ were then ball milled for 10 hours with an increasing amount of $VNbO_5$, namely, 5 wt%, 10 wt% and 15 wt%. In order to evaluate the effect of $VNbO_5$, temperature programmed desorption (TPD) measurements of the samples were recorded and compared in Fig. 2. The TPD profiles reported in Fig. 2a, revealed a similar dehydrogenation behavior, with all the samples releasing hydrogen in a single step. On the other hand, the onset desorption temperatures of the doped and un-doped composites, decreased simultaneously with the increasing amount of $VNbO_5$. The un-doped $MgH_2$ started to release hydrogen at around 330 °C, with a total amount of 6.67 wt% reached at 400 °C, lower than the expected theoretical gravimetric capacity (7.6 wt%). This reduction was probably due to the presence of MgO impurities in the starting material and to the partial hydrogen release induced by the high-energy ball milling during the preparation. Compared to the un-milled $MgH_2$, the onset temperature was decreased by 100 °C in agreement with previous studies.[40] When $MgH_2$ was milled with 5 wt% of $VNbO_5$, the temperature release of hydrogen further decreased to 270 °C with a total dehydrogenation of 6.27 wt% $H_2$ at 400 °C. For the samples doped with 10 wt% and 15 wt% of $VNbO_5$, the onset desorption temperatures were reduced to 264 °C (6.07 wt% – 400 °C) and 234 °C (5.89 wt% – 400 °C), respectively. The total amount of hydrogen evolved from these doped systems, at 400 °C, was lower if compared with the un-doped $MgH_2$. However, considering their theoretical capacity, they desorbed 86 (5 wt%), 87 (10 wt%) and 89% (15 wt%) respectively.

In order to better evaluate the different TPD results, the 1st derivative of the desorption profiles was calculated and reported in Fig. 2b. The inspection of the first derivative allowed determining the maximum desorption peak and helped in distinguishing multiple desorption processes when they occur consecutively and/or very close to one another. The graph confirmed the trend observed for the integral desorption curves, with a reduction of the onset desorption temperatures when the additive content was increased. The same trend was observed for the hydrogen desorption peak maxima. In fact, the un-doped $MgH_2$ sample started to release hydrogen at 330 °C, with a peak maximum centred at 349 °C. For the 5 wt%, 10 wt% and 15 wt% doped samples, the peak temperatures of 320 °C, 297 °C and 277 °C were observed. The latter result is quite interesting because the dehydrogenation step occurred in a range between 230 and 300 °C. Note that, at these temperatures, pristine $MgH_2$ is quite stable, suggesting a large destabilization due to the presence of $VNbO_5$. This insight appears to be of major interest if compared with the results obtained by the addition of other transition metal mixed oxides. For example, the addition of $CoFe_2O_4$, $ZnFe_2O_4$, $MnFe_2O_4$ and $Mn_{0.5}Zn_{0.5}Fe_2O_4$ nanoparticles on $MgH_2$, improved significantly the sorption kinetics only at temperatures higher than 300 °C, with the maximum peaks located around 330–350 °C.[41]

The de-hydrogenated composites doped with 10 wt% and 15 wt% of $VNbO_5$ were re-hydrogenated and then subjected to a new heating ramp from room temperature to 300 °C. In Fig. 3a,

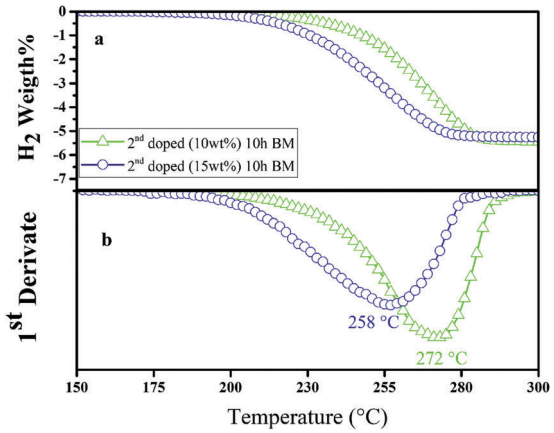


Fig. 3 (a) 2nd TPD profiles of $MgH_2$ doped with 10 wt% (green triangles) and 15 wt% (blue circles) of $VNbO_5$. (b) 1st derivate of the TPD measurements reported in panel (a).

the second desorption cycle *versus* the heating temperature, is reported. An onset temperature of 200 °C was observed for both the doped samples, with a decrease of 60 °C (15 wt%) and 30 °C (10 wt%), if compared to the first step. In addition, hydrogen gas was completely released at 285 °C.

The derivative plot, depicted in Fig. 3b, confirmed the data observed in the previous analysis. Focusing on the hydrogen storage properties, the sample doped with 15 wt% of $VNbO_5$ released 50% of hydrogen at 250 °C and 99% at 275 °C. As clearly shown in Fig. 4, the second desorption event of the 10 wt%-doped sample was lower compared to that of the 15 wt% sample, but significantly higher with respect to the first desorption in the whole range of temperatures analysed. This also confirmed the beneficial effect of the activation process in the composites, although further structural investigations are necessary to confirm this point.

Concerning the absorption analysis, reported in Fig. 5a, the systems with 5 wt%, 10 wt% and 15 wt% of $VNbO_5$ stored a maximum of 4.60, 5.58 and 5.34 wt% of hydrogen, respectively, after 60 minutes. This is a significant improvement if compared with the un-doped $MgH_2$ system able to re-absorb only 1.5 wt% of hydrogen after 60 minutes. However, different sorption kinetics were evidenced during the first 30 minutes; in particular, the samples doped with 10 wt% and 15 wt% of $VNbO_5$ absorbed more than the 5 wt% of hydrogen, higher with respect to the 4.4 wt% $H_2$ observed in the 5 wt%-doped samples.

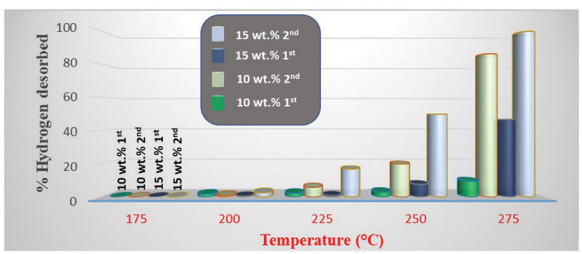


Fig. 4 Percentage of the total hydrogen released during the first and second desorption step of the $MgH_2$ doped with 10 and 15 wt% of $VNbO_5$, as a function of the temperature ramp. The green (1st des step) and light green (2nd des step) cylinders refer to the 10 wt% doped sample, whereas the dark blue (1st des step) and sky blue (2nd des step) cylinders refer to the 15 wt% doped sample. The percentage values have been calculated starting from the total amount of hydrogen evolved experimentally from each sample.

The sample with 15 wt% of additive, confirmed the best performance observed in the desorption investigation (see Fig. 5b): 50% of the total hydrogen was absorbed in just 1.25 minutes while 5 minutes were required to reach 90% of the theoretical amount under the moderate conditions 160 °C and 20 bar of $H_2$. For comparison, the sample with 10 wt% of $VNbO_5$, absorbed 15 and 72% after 1.25 and 5 minutes, respectively.

Based on these promising results, the investigation then focused on the $MgH_2$ doped with 15 wt% of $VNbO_5$ in order to evaluate its performance for several ab–desorption cycles (50). The amount of $H_2$ (wt%) charged and dis-charged *versus* the cycle number for three different working temperatures (250 °C, 275 °C and 300 °C) is shown in Fig. 6. At 300 °C (red squares in Fig. 6a), the sample stored reversibly over 5–5.5 wt% of $H_2$ for 50 cycles.

At the lower temperature of 275 °C (green squares in Fig. 6b), the system stored reversibly a significant amount of 5–5.25 wt% $H_2$ for 72 cycles. This result indicated the high stability of the composite under these operative conditions. On the other hand, at 250 °C (blue squares in Fig. 6c), after the 10th cycle, the system ab/desorbed only 3 wt% of hydrogen and below 2 wt% upon the 20th cycle.

To integrate the results obtained during the cyclability experiments on the 15 wt%-doped system, the hydrogen rate values achieved at 300 °C are reported in Table 1 and compared to those obtained under similar conditions for other high-performing magnesium-catalysed systems presented in the recent literature.[25,42–45]

As clearly emerged from the data reported in Table 1, the kinetics rates achieved with the addition of $VNbO_5$ were significantly higher than those obtained in the $MnFe_2O_4$-, $Cr_2O_3$-, Ni- and $Nb_2O_5$/$Cr_2O_5$-based systems. Furthermore, a substantial enhancement could be also observed with respect to the $Nb_2O_5$- and V-catalysed systems for both the hydrogenation steps, supporting a synergetic effect when the two compounds are combined.

With the aim of investigating the crystalline phases in the 15 wt%-doped system during the cycling experiments conducted at 275 °C, X-ray diffraction patterns were recorded on the crystalline powders after the desorption and absorption steps, and compared with the as-milled mixture. As shown in Fig. 7, in the initial system, the ball milling promoted a partial conversion of β-$MgH_2$ ($\langle D \rangle$ 140 ± 5 Å) in the γ-$MgH_2$ ($\langle D \rangle$ 180 ± 5 Å) polymorph. Furthermore, the presence of nanocrystalline MgO (<5 wt%) was also observed. No peaks ascribable to Nb- or V-related phases were detected in the initial pattern. $VNbO_5$ reflections could not be observed due to the nanostructuring process induced by the mechanical treatment. The XRD analysis on the powders upon desorption (275 °C) revealed the presence of 91 wt% of Mg metallic ($\langle D \rangle$ 1100 ± 10 Å) together with 7 wt% of nanocrystalline MgO ($\langle D \rangle$ 90 ± 5 Å). The peaks related to γ-$MgH_2$ completely disappeared while traces of β-$MgH_2$ (<2 wt%) were still detectable. This was apparently in

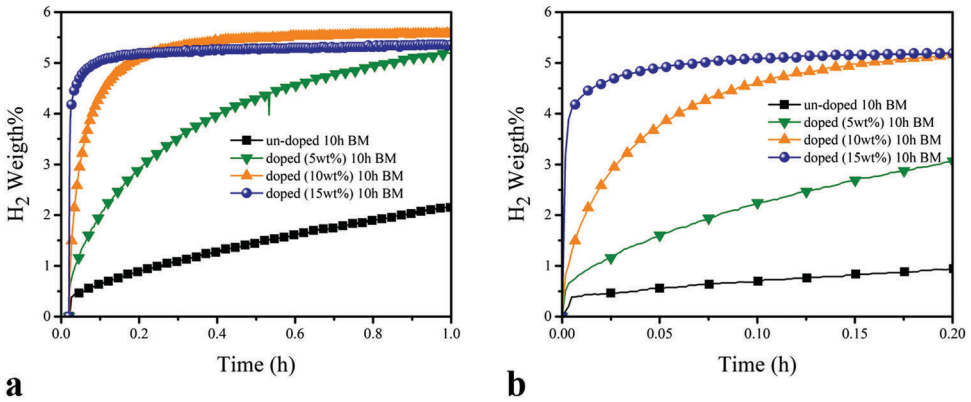


Fig. 5 (a) Absorption profiles recorded at 160 °C and 20 bar of $H_2$ of the un-doped and doped $MgH_2$. (b) Zoom panel of the absorption profile in the first 10 minutes.

contrast with the plateau reached in the volumetric measurements for the catalysed-systems. However, the $H_2$ evolved upon the desorption step in the reactor, was probably enough to react with the dehydrogenated powders before being evacuated at room temperature for the XRD measurements. Concerning MgO, its presence could be explained by the long-time collection (12 h) of the patterns necessary for achieving a reasonable pattern suitable for the Rietveld refinement. Furthermore, a contribution from the $VNbO_5$ cannot be excluded although no evidence for the crystalline V- or Nb- or related phases were visible in the diffraction pattern. It is also important to highlight that the amount of MgO extrapolated from the quantitative analysis was in line with the experimental measurements of the evolved hydrogen and its strong peaks emerged because the log × $q$ scale was used for the intensity, emphasizing smaller reflections. Similar conclusions could also be made for the pattern collected on the powders after re-absorption (275 °C) and visualized in Fig. 7. β-$MgH_2$ ($\langle D \rangle$ 900 ± 10 Å) was the main phase observed in the final pattern (90 wt%) with a trace of unreacted Mg (<3 wt%) and MgO (<7 wt%).

### Kinetics and thermodynamic investigations

The analysis of the microstructure parameters of the patterns reported in Fig. 7, evidenced that after cycling the crystallite dimensions of the β-$MgH_2$ phase increased significantly while the hydrogen storage performances of the whole system were preserved (see Fig. 6). This means that the initial nanostructured conditions of the system did not influence the performance of the $MgH_2$–15 wt% $VNbO_5$ sample. In other words, the activity of the $VNbO_5$ additive should play a central role for enhancing the hydrogen storage properties of $MgH_2$. Based on this consideration, in order to better evaluate the effect of the additive, the activation energy of the 15 wt%-doped system, has been evaluated by the Kissinger method using the following equation:[46]

$$\frac{\mathrm{d}\ln\left(\frac{\beta}{T_\mathrm{m}^2}\right)}{\mathrm{d}\left(\frac{1}{T_\mathrm{m}}\right)} = -\frac{E_\mathrm{a}}{R} \quad (1)$$

where $\beta$ corresponds to the heating rate, $T_\mathrm{m}$ is the peak temperature and $R$ is the gas constant.

DSC profiles, reported in Fig. 8, were recorded for the un-doped (panel a) and doped systems (panel b), by varying the heating rate (2, 5, 10, 15 and 20 °C). As expected, the endothermic peaks corresponding to the maximum rate of dehydrogenation shifted to higher temperatures as the heating rate was increased for both the samples.

For all the heating rates, the hydrogen release onset and peak maximum started at lower temperatures for the doped systems, corroborating the previous results obtained using a manometric apparatus. The discrepancy temperatures with respect to the TPD experiments (static vacuum), were due to the different pressure conditions used in the DSC analysis (1 bar Ar). The plot based on the Kissinger equation (eqn (1)), is shown in Fig. 9.

A good linear relationship between $\ln(\beta/T_{\max}^2)$ and $1/T_{\max}$ was obtained for all the samples, allowing calculating the activation energy of dehydrogenation from the slope of the straight lines. The activation energies are summarized in Table 2 together with several values reported in the current literature for the $MgH_2$-doped systems.[26,44,47–57]

It should be noted that the $VNbO_5$-doped system showed a lower activation energy with respect to the un-doped system (99 *vs.* 115 kJ $mol^{-1}$), proving that its faster hydrogen desorption kinetics was strictly correlated with the action of the dopant. Furthermore, the value extrapolated for the $VNbO_5$-doped system was similar,[47] and in most of the cases significantly lower[26,48–50,53–56] if compared with those of the most promising additives reported in the recent literature. As for the kinetics rate, the system milled with the ternary oxide $VNbO_5$ reported a higher destabilization than the V-[49] and $Nb_2O_5$-catalyzed[26] systems. On the other hand, a Ti-doped sample, investigated by Zhu and co-authors,[57] exhibited an extraordinary lower activation energy of 31 kJ $mol^{-1}$ $H_2$, when compared with the $VNbO_5$-doped system here reported. However, in the former case, the catalyst was introduced by the coating technique instead of mechanical treatment, with the disadvantage of supplying solvent reagents and increasing the cost of

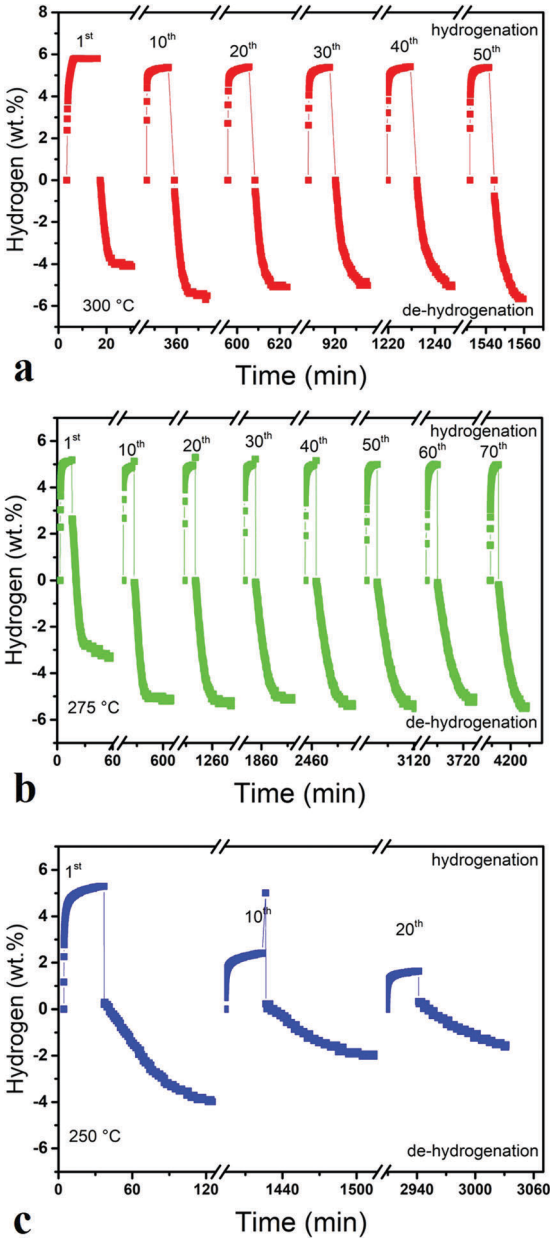


Fig. 6 Amount of hydrogen (wt%) ab/desorbed in the $MgH_2$ doped with 15 wt% of $VNbO_5$ as a function of the cycle number performed at 300 °C (panel a), 275 °C (panel b) and 250 °C (panel c). The desorption was carried out under static vacuum (45 minutes) and the absorption under 20 bar of $H_2$ (10 minutes).

production. A lower value of the activation energy (65 kJ $mol^{-1}$ $H_2$), although not comparable with the previous case, was obtained by Li *et al.*, when $MnFe_2O_4$ was added to $MgH_2$.[44] This very interesting value was not confirmed by a recent work published by Ismail and co-authors (108), despite the clear benefit, in terms of sorption kinetic, achieved by introducing this ternary oxide.[58]

Considering the weighting impact of $VNbO_5$ on the hydrogen sorption kinetics of $MgH_2$, it was also relevant to investigate the relative thermodynamic stability of the 15 wt%-doped system. For this specific purpose, PCI curves (Fig. 10) were

Table 1 Hydrogen kinetic rate values (wt% $H_2$ $min^{-1}$) of several catalysed $MgH_2$ systems obtained for the desorption and absorption steps at 300 °C

| Additive | Desorption at 300 °C (wt% $H_2$ $min^{-1}$) | Absorption at 300 °C (wt% $H_2$ $min^{-1}$) |
|---|---|---|
| $VNbO_5$ | 1.49 | 3.46 |
| Ni[42] | 0.03 | 1.86 |
| V[42] | 1.66 | — |
| $Cr_2O_3$[43] | 0.07 | 1.17 |
| $MnFe_2O_4$[44] | 0.08 | — |
| $Nb_2O_5$[45] | 2.50 | 3.00 |
| $Nb_2O_5$ + $Cr_2O_5$[25] | 0.25 | 1.20 |

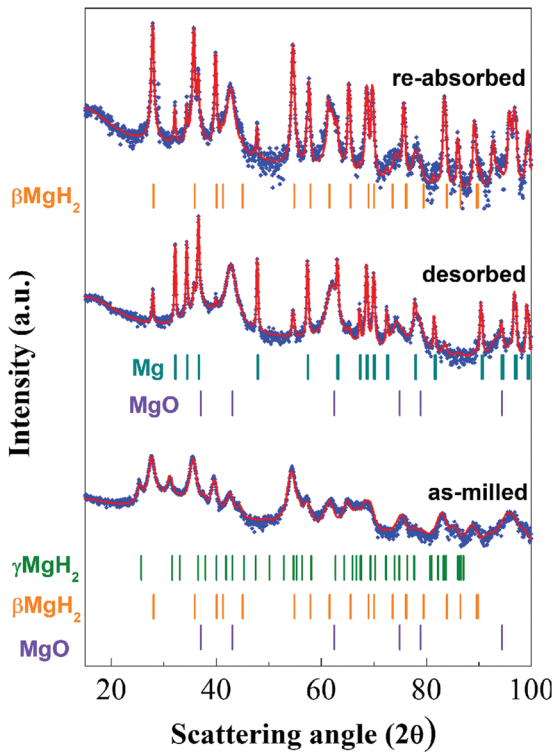


Fig. 7 Experimental (blue squares) and Rietveld refined (red solid line) XRD patterns of the 15 wt%-doped $MgH_2$ after the desorption and absorption steps (5th cycle). XRD pattern of the as-milled system is also shown for comparison.

recorded on the doped compound at 275 °C, 300 °C and 325 °C for the desorption (panel a) and absorption (panel b) steps.

PCI curves were characterized by a singular plateau pressure, confirming the equilibrium reaction (R1):

$$MgH_2(cat) \leftrightarrow Mg(cat) + H_2 \quad (R1)$$

Any other structural event related to the formation of MgV or MgNb could be then excluded, suggesting, again, the stability of the catalyst.

For all the temperatures analysed, roughly 5 wt% of hydrogen was desorbed and absorbed, although the system measured at 275 °C showed the lower equilibrium pressures of 0.87 and 1.81 bar for the desorption and absorption curves, respectively. The total equilibrium pressure $P_{eq}$ was calculated

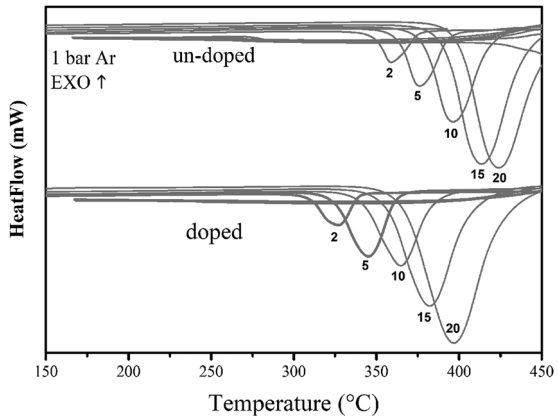


Fig. 8 DSC curves of the un-doped (panel a) and doped (panel b) $MgH_2$ recorded at different heating ramps of 2 °C $min^{-1}$; 5 °C $min^{-1}$, 10 °C $min^{-1}$, 15 °C $min^{-1}$ and 20 °C $min^{-1}$.

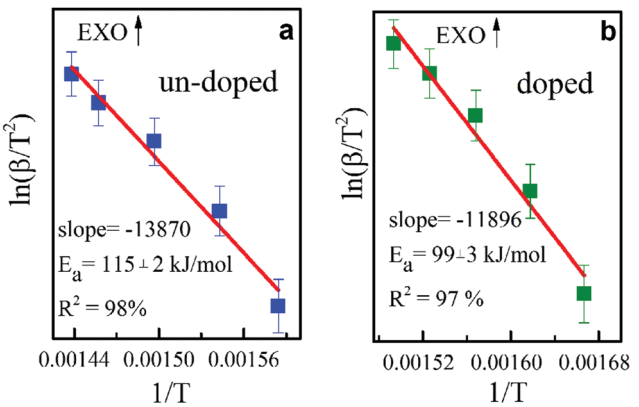


Fig. 9 Kissinger plots and the related activation energy ($E_a$) values of the un-doped and 15 wt% $VNbO_5$-doped $MgH_2$.

starting from the plateau pressure values extrapolated from the absorption and desorption profiles using eqn (2):[59]

$$P_{eq} = \sqrt{P_{des} P_{abs}} \quad (2)$$

The equilibrium pressure can be correlated to the enthalpy of reaction by the Van't Hoff eqn (3):

$$\ln \frac{P_{eq}}{P_0} = \frac{\Delta G}{RT} = \frac{\Delta H}{RT} - \frac{\Delta S}{R} \quad (3)$$

From the intercept and slope of $\ln P_{eq}/P_0$ *versus* $1/T$ (Van't Hoff plot), the entropy and enthalpy values of $MgH_2$–15 wt% $VNbO_5$ were derived. As reported in Fig. 11, the change of the enthalpy and entropy of the reaction (R1) was 70.65 ± 0.43 kJ $mol^{-1}$ $H_2$ and 114.73 ± 0.75 J K $mol^{-1}$ $H_2$, respectively.

Comparing the enthalpy of reaction values obtained with those of the pure $MgH_2$ (77 kJ $mol^{-1}$ $H_2$[60]) and according to those of other doped $ZrF_4$-[61] (75 kJ $mol^{-1}$ $H_2$), $NbF_5$-[61] (77 kJ $mol^{-1}$ $H_2$), $TaF_5$-[61] (75 kJ $mol^{-1}$ $H_2$), $TiCl_3$-[61] (73 kJ $mol^{-1}$ $H_2$) and $SrTiO_3$-[62] (77 kJ $mol^{-1}$ $H_2$) samples, it was possible to conclude that the addition of $VNbO_5$ apparently did not modify significantly the thermodynamic properties of $MgH_2$, but acted as an effective dopant with a clear reduction of the activation energy.

Table 2 Activation energy ($E_a$) values (kJ $mol^{-1}$) of several $MgH_2$-doped systems

| Additive | $E_a$ (kJ $mol^{-1}$) |
|---|---|
| $VNbO_5$ | 99 |
| $MgH_2$ milled 10 h | 115 |
| Pure $MgH_2$[47] | 174 |
| $FeCl_3$[48] | 130 |
| V[49] | 119 |
| $TiH_2$[47] | 131 |
| $Mg_2Ni$[47] | 98 |
| C + $Nb_2O_5$[26] | 102 |
| Ni + rGO[50] | 108 |
| $Cr_2O_3$[51] | 86 |
| $MnFe_2O_4$[44,58] | 65, 108 |
| Ni[52] | 75 |
| $BiVO_4$[34] | 84 |
| $Co_2NiO$[53] | 118 |
| $TiO_2$[54] | 111 |
| $CeO_2$[55] | 109 |
| $SrFe_{12}O_{19}$[56] | 114 |
| Ti[57] | 37 |

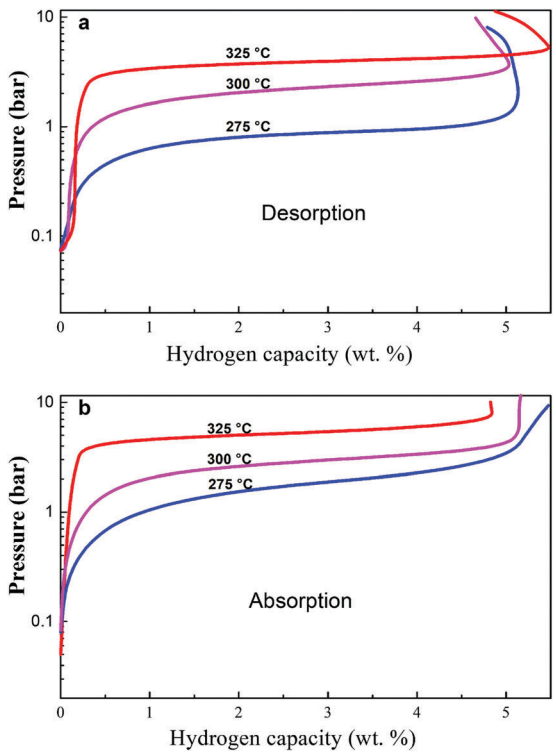


Fig. 10 PCI desorption (a) and absorption (b) curves of $MgH_2$–15 wt% $VNbO_5$ determined at different temperatures.

## Conclusions

In this work, the catalytic effect of the as-synthesized $VNbO_5$ on the sorption properties of $MgH_2$ was, for the first time, experimentally investigated in detail. The addition of the catalyst, added in different concentrations (5, 10 and 15 wt%), allowed

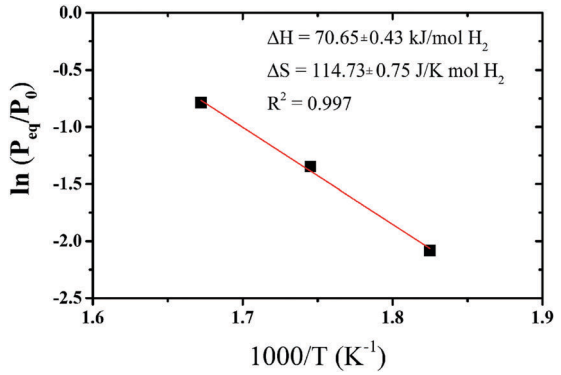


Fig. 11 Van't Hoff plot for the $MgH_2$–15 wt% $VNbO_5$ system.

reducing the desorption temperature of $MgH_2$ down to 280 °C, which could be further decreased to 220 °C after the first hydrogenation cycle. Among the doped systems, the best performing composite was the 15 wt%-doped one, which showed a total absorption of 5.5 wt% of hydrogen in 10 minutes at 160 °C under 20 bar of hydrogen, and full reversibility was achieved at a temperature of 275 °C for more than 50 cycles. Structural and microstructural characterization was performed using X-ray diffraction on the ab-dehydrogenated powders. The analysis of the pattern profiles, performed using Rietveld refinement, proved a good dispersion of the catalyst in the whole system and without the formation of any secondary undesired phase. In order to quantify the kinetic barrier and thermodynamic stability of the catalysed-powders, the activation energy and the reaction enthalpy have been experimentally derived. The activation energy, $E_a$, calculated from the desorption process (99 kJ $mol^{-1}$), was significantly lower if compared to the 115 kJ $mol^{-1}$ values obtained for the un-doped sample. Compared with many other dopants such as $FeCl_3$ (112 kJ $mol^{-1}$), V (119 kJ $mol^{-1}$), $TiH_2$ (131 kJ $mol^{-1}$), $Nb_2O_5$ (102 kJ $mol^{-1}$) and Ni + rGO (108 kJ $mol^{-1}$), the $VNbO_5$ dopant showed a superior catalytic activity for destabilizing the decomposition of $MgH_2$. Considering the thermodynamic stability, the doped system reported a reaction enthalpy of ~71 kJ $mol^{-1}$ $H_2$ similar to that obtained for the pure $MgH_2$. This value together with the linear equilibrium plateau achieved for the PCI curves collected at three different temperatures, confirmed that $VNbO_5$ plays a crucial role in the kinetic destabilization of the $MgH_2$ system.

From the findings reported in this manuscript it emerged that although the working temperature of 275 °C was significantly lowered with respect to the pure $MgH_2$ (400 °C), it is still too high for PEM fuel cell powdered vehicles. However, the very fast kinetics rate achieved, among the best in the current literature, and the high number of cycles sustained, proves this system is a very promising candidate for off-board applications such as grid energy storage.

## Conflicts of interest

## Acknowledgements

This work was supported by the University of Sassari and MIUR (Italian Ministry for University and Research).

## Notes and references

1 T. R. Karl, J. M. Melillo and T. C. Peterson, *Global Climate Change Impacts in the United States*, Cambridge University Press, 2009.
2 S. Moroz, X. F. Tan, J. Pierce, M. Greaves, A. Duguid, K. Dumur and J. Ng, *J. Alloys Compd.*, 2013, **580**, S329–S332.
3 DOE, *Target Explanation Document: Onboard Hydrogen Storage for Light-Duty Fuel Cell Vehicles*, 2015, **7**.
4 J. C. Crivello, R. V. Denys, M. Dornheim, M. Felderhoff, D. M. Grant, J. Huot, T. R. Jensen, P. de Jongh, M. Latroche, G. S. Walker, C. J. Webb and V. A. Yartys, *Appl. Phys. A: Mater. Sci. Process.*, 2016, **122**, 2.
5 I. Dovgaliuk and Y. Filinchuk, *Int. J. Hydrogen Energy*, 2016, **41**, 15489–15504.
6 H. T. Hwang and A. Varma, *Curr. Opin. Chem. Eng.*, 2014, **5**, 42–48.
7 C. Pistidda, N. Bergemann, J. Wurr, A. Rzeszutek, K. T. Møller, B. R. S. Hansen, S. Garroni, C. Horstmann, C. Milanese, A. Girella, O. Metz, K. Taube, T. R. Jensen, D. Thomas, H. P. Liermann, T. Klassen and M. Dornheim, *J. Power Sources*, 2014, **270**, 554–563.
8 O. Friedrichs, J. C. Sánchez-López, C. López-Cartes, M. Dornheim, T. Klassen, R. Bormann and A. Fernández, *Appl. Surf. Sci.*, 2006, **252**, 2334–2345.
9 N. Takeichi, K. Tanaka, H. Tanaka, T. T. Ueda, Y. Kamiya, M. Tsukahara, H. Miyamura and S. Kikuchi, *J. Alloys Compd.*, 2007, **446–447**, 543–548.
10 S. Garroni, C. Pistidda, M. Brunelli, G. B. M. Vaughan, S. Suriñach and M. D. Baró, *Scr. Mater.*, 2009, **60**, 1129–1132.
11 S. Garroni, C. Milanese, A. Girella, A. Marini, G. Mulas, E. Menéndez, C. Pistidda, M. Dornheim, S. Suriñach and M. D. Baró, *Int. J. Hydrogen Energy*, 2010, **35**, 5434–5441.
12 C. Pistidda, S. Garroni, C. B. Minella, F. Dolci, T. R. Jensen, P. Nolis, U. Bösenberg, Y. Cerenius, W. Lohstroh, M. Fichtner, M. D. Baró, R. Bormann and M. Dornheim, *J. Phys. Chem. C*, 2010, **114**, 21816–21823.
13 C. B. Minella, S. Garroni, C. Pistidda, G. Barkhordarian, C. Rongeat, I. Lindemann, O. Gutfleisch, T. R. Jensen, Y. Cerenius, I. Christensen, M. D. Baró, R. Bormann, T. Klassen and M. Dornheim, *J. Phys. Chem. C*, 2011, **115**, 2497–2504.
14 C. Milanese, S. Garroni, A. Girella, G. Mulas, V. Berbenni, G. Bruni, S. Suriñach, M. D. Baró and A. Marini, *J. Phys. Chem. C*, 2011, **115**, 3151–3162.
15 B. Zahiri, M. Danaie, X. Tan, B. S. Amirkhiz, G. A. Botton and D. Mitlin, *J. Phys. Chem. C*, 2012, **116**, 3188–3199.
16 C. Milanese, A. Girella, S. Garroni, G. Bruni, V. Berbenni, P. Matteazzi and A. Marini, *Int. J. Hydrogen Energy*, 2010, **35**, 1285–1295.

 

17 C. Ren, Z. Z. Fang, C. Zhou, J. Lu, Y. Ren and X. Zhang, *J. Phys. Chem. C*, 2014, **118**, 21778–21784.

18 F. Cova, F. Gennari and P Arneodo Larochette, *Int. J. Hydrogen Energy*, 2014, **39**, 11501–11508.

19 S. Deledda, A. Borissova, C. Poinsignon, W. J. Botta, M. Dornheim and T. Klassen, *J. Alloys Compd.*, 2005, **404–406**, 409–412.

20 S. A. Jin, J. H. Shim, J. P. Ahn, Y. W. Cho and K. W. Yi, *Acta Mater.*, 2007, **55**, 5073–5079.

21 Y. Luo, P. Wang, L. P. Ma and H. M. Cheng, *J. Alloys Compd.*, 2008, **453**, 138–142.

22 G. Barkhordarian, T. Klassen and R. Bormann, *Scr. Mater.*, 2003, **49**, 213–217.

23 G. Barkhordarian, T. Klassen and R. Bormann, *J. Alloys Compd.*, 2004, **364**, 242–246.

24 O. Friedrichs, T. Klassen, J. C. Sánchez-López, R. Bormann and A. Fernández, *Scr. Mater.*, 2006, **54**, 1293–1297.

25 A. Patah, A. Takasaki and J. S. Szmyd, *Int. J. Hydrogen Energy*, 2009, **34**, 3032–3037.

26 C. Milanese, A. Girella, S. Garroni, G. Bruni, V. Berbenni, P. Matteazzi and A. Marini, *Int. J. Hydrogen Energy*, 2010, **35**, 9027–9037.

27 H. G. Schimmel, J. Huot, L. C. Chapon, F. D. Tichelaar and F. M. Mulder, *J. Am. Chem. Soc.*, 2005, **127**, 14348–14354.

28 O. Friedrichs, F. Aguey-Zinsou, J. R. A. Fernández, J. C. Sánchez-López, A. Justo, T. Klassen, R. Bormann and A. Fernández, *Acta Mater.*, 2006, **54**, 105–110.

29 O. Friedrichs, J. C. Sánchez-López, C. López-Cartes, T. Klassen, R. Bormann and A. Fernández, *J. Phys. Chem. B*, 2006, **110**, 7845–7850.

30 O. Friedrichs, D. Martínez-Martínez, G. Guilera, J. C. S. López and A. Fernández, *J. Phys. Chem. C*, 2007, **111**, 10700–10706.

31 F. Dolci, M. Baricco, P. P. Edwards and E. Giamello, *Int. J. Hydrogen Energy*, 2008, **33**, 3085–3090.

32 W. Oelerich, T. Klassen and R. Bormann, *J. Alloys Compd.*, 2001, **322**, L5–L9.

33 D. Korablov, T. K. Nielsen, F. Besenbacher and T. R. Jensen, *Powder Diffr.*, 2015, **30**, S9–S15.

34 G. Xu, N. Shen, L. Chen, Y. Chen and W. Zhang, *Mater. Res. Bull.*, 2017, **89**, 197–203.

35 Z. C. Wang, J. W. Liu, M. Schlangen, T. Weiske, D. Schroder, J. Sauer and H. Schwarz, *Chem. – Eur. J.*, 2013, **19**, 11496–11501.

36 P. Tabero, E. Filipek and M. Piz, *Open Chem.*, 2009, **7**, 222–227.

37 C. Börrnert, W. Carrillo-Cabrera, P. Simon and H. Langbein, *J. Solid State Chem.*, 2010, **183**, 1038–1045.

38 H. Langbein and T. Mayer-Uhma, *Mater. Res. Bull.*, 2009, **44**, 654–659.

39 P. Scardi, L. Lutterotti and P. Maistrelli, *Powder Diffr.*, 1994, **9**, 180–186.

40 A. Motavalli, M. Rajabi and A. Gholipoor, *J. Adv. Mater. Proc.*, 2014, **2**, 67–72.

41 J. Zhang, J. Shan, P. Li, F. Zhai, Q. Wan, Z. Liu and X. Qu, *J. Alloys Compd.*, 2015, **643**, 174–180.

42 R. A. Varin, T. Czujko, E. B. Wasmund and Z. S. Wronski, *J. Alloys Compd.*, 2007, **432**, 217–231.

43 M. Song, J. L. Bobet and B. Darriet, *J. Alloys Compd.*, 2002, **340**, 256–262.

44 P. Li, Q. Wan, Z. Li, F. Zhai, Y. Li, L. Cui, X. Qu and A. A. Volinsky, *J. Power Sources*, 2013, **239**, 201–206.

45 P. A. Huhn, M. Dornheim, T. Klassen and R. Bormann, *J. Alloys Compd.*, 2005, **404–406**, 499–502.

46 H. E. Kissinger, *Anal. Chem.*, 1957, **432**, 1702–1706.

47 S. T. Sabitu, O. Fagbami and A. Goudy, *J. Alloys Compd.*, 2011, **509**, S588–S591.

48 M. Ismail, *Int. J. Hydrogen Energy*, 2014, **39**, 2567–2574.

49 T. Liu, T. Zhang, C. Qin, M. Zhu and X. Li, *J. Power Sources*, 2011, **196**, 9599–9604.

50 G. Liu, Y. Wang, F. Qiu, L. Li, L. Jiao and H. Yuan, *J. Mater. Chem.*, 2012, **22**, 22542.

51 M. Polanski and J. Bystrzycki, *J. Alloys Compd.*, 2009, **486**, 697–701.

52 M. S. El-Eskandarany, E. Shaban, N. Ali, F. Aldakheel and A. Alkandary, *Sci. Rep.*, 2016, **6**, 37335.

53 N. Juanhir, N. S. Mustafa, A. M. Sinin and M. Ismail, *RSC Adv.*, 2015, **5**, 60983.

54 D. Pukazhselvan, N. Nasani, P. Correia, E. Carbo-Argibay, G. Otero-Irurueta, D. G. Stroppa and D. P. Fagg, *J. Power Sources*, 2017, **362**, 174–183.

55 N. S. Mustafa and M. Ismail, *J. Alloys Compd.*, 2017, **695**, 2532–2538.

56 N. S. Mustafa, N. N. Sulaiman and M. Ismail, *RSC Adv.*, 2016, **6**, 110004.

57 J. Cui, H. Wang, J. Liu, L. Ouyang, Q. Zhang, D. Sun, X. Yao and M. Zhu, *J. Mater. Chem. A*, 2013, **1**, 5603–5611.

58 N. H. Idris, N. S. Mustafa and M. Ismail, *Int. J. Hydrogen Energy*, 2017, **42**, 21114.

59 N. Patelli, M. Calizzi, A. Migliori, V. Morandi and L. Pasquini, *J. Phys. Chem. C*, 2017, **121**, 11166–11177.

60 J. J. Reilly and R. H. Wiswall, *Inorg. Chem.*, 1968, **7**, 2254–2256.

61 I. E. Malka, M. Pisarek, T. Czujko and J. Bystrzycki, *Int. J. Hydrogen Energy*, 2011, **36**, I2909–I2917.

62 M. S. Yahya and M. Ismail, *J. Energy Chem.*, 2017, DOI: 10.1016/j.jechem.2017.10.020. Q14